Slip Velocity and Drag Law in a Liquid-Liquid Homogeneous Dispersed Flow

Frédéric Augier, Olivier Masbernat, and Pascal Guiraud
Laboratoire de Génie Chimique, UMR 5503 CNRS/INPT/UPS, 31106 Toulouse cedex 1, France

Local measurements of phase velocities and phase fraction in a dense liquid-liquid homogeneous flow were done based on an application of PIV with a refractive index matching technique. This technique allowed to measure simultaneously both phase velocities and phase fraction fields, as well as the drop mean diameter in a vertical cocurrent flow of n-heptane dispersed in an aqueous solution of glycerin. The evolution of the relative velocity as a function of the phase fraction (0−0.4) was studied with moderate particle Reynolds numbers (10−100) for drops behaving as spherical rigid particles. A local drag coefficient was derived from these measurements. The calculated mean relative velocity as a function of the local phase fraction with existing classical drag coefficient laws showed significant discrepancies with the measurements overestimated. Thus, the drag coefficient variation rate as a function of the phase fraction was underestimated by the models. The evolution of the normalized velocity (by the terminal velocity) as a function of the phase fraction was predicted correctly with mixture viscosity models in a creeping flow regime.

Introduction

The application of statistically averaged two-fluid models for the simulation of complex industrial two-phase flows requires the development of adequate models for the interfacial momentum exchange. This task becomes problematic at a high phase fraction of the dispersed phase. The quality of the prediction of the mean velocity and phase fraction profiles strongly depends upon the interfacial momentum exchange term, starting with the stationary drag force. In the case of buoyancy driven two-phase flows (vertical columns, fluidized, or circulating beds), this force builds the main contribution balancing the buoyancy force. Two-phase turbulence transport also involves the characteristic drag time of the dispersed phase, which scales the terms of production or dissipation of fluctuations of both phases, as well as the fluid-particle fluctuations covariance (Simonin, 1991). An accurate modeling of the drag force is, therefore, a very important issue regarding the prediction of mean and turbulent features of two-phase flows, and this problem has provided an appreciable amount of literature. Concerning liquid-liquid flows, Barnea and Mezrahi (1975) extended a drag coefficient law obtained with solid-fluid systems to liquid-liquid systems using the concept of effective viscosity (Hadamard-Rybsczinski correction) and a mixture viscosity law validated at a high phase fraction (extension of a Taylor linear law). They tested their model in a wide range of particle Reynolds number and phase fraction against 12 different experimental data sources obtained from fluidized or settling spherical drops in liquid-liquid systems. They found a maximum deviation of 7% on the relative velocity between the phases. Using the same concept of mixture viscosity, Ishii and Zuber (1979) also derived a drag law for particulate flows, for gas-liquid as well as for liquid-liquid systems, including the case of distorted inclusions. They also reached a good level of prediction of experimental slip velocity in a wide range of flow parameters. Kumar and Hartland (1985) have proposed an empirical drag law specific to liquid-liquid systems based on a large number of experimental data (nearly 1,000 data for nearly 30 different liquid-liquid systems) covering an important range of particle Reynolds and Eötvös numbers and of phase fraction. Without going into the details of these laws and analyzing their behavior, it is important to point out that these drag laws and others are used as a local model of the stationary drag term to be implemented into CFD two-phase codes. The

Correspondence concerning this article should be addressed to O. Masbernat.

significant discrepancies observed between the proposed drag coefficient models (Rushe and Issa, 2000) raises the question of the choice of a particular drag law for a given liquid-liquid application. Therefore, in order to evaluate a drag law for a given two-phase flow application, it seems necessary to test it on the basis of statistically averaged local measurements of the drag force. The classical method to measure the drag force in a dispersed flow is to measure both phase velocity and phase fractions within a vertical homogeneous dispersed flow. In the absence of gradient of mean velocity, phase fraction, and Reynolds stress, the momentum balance at steady state reduces to equilibrium between the drag and the buoyancy forces. As discussed below, in many cases taken from the literature, the measurements were performed on a global scale of the dispersed flow including possible wall or boundary effects or recirculation patterns. Slip velocity, phase fraction, and drop size data were collected in fluidized systems (zero flow rate of the dispersed phase), gravity settlers (zero flow rate of the continuous phase), and cocurrent or countercurrent flows. Weaver et al. (1959), Hazlebeck and Geankoplis (1963), and Geankoplis et al. (1982) have studied different water-organic phase systems in a spray tower. Phase fractions and velocities were measured with a "quick closing valves" method that allows to isolate a large zone of the column in a short period of time. The phase fraction was then determined by measuring the volumes occupied by each phase after settling. Phase velocities were deduced from the measurements of the phase fractions and of the flow rates (before closing the valves at the upper and lower boundaries of the column volume). For more details about this method and others, see Kumar et al. (1996). In these studies, drop diameters were measured using a photographic method. Pictures of the drops close to the walls were taken and analyzed. Garwin and Smith (1953) have studied some water-benzene flows in the same kind of geometry, but with a zero continuous phase flow rate, and manually measuring the velocity of drops along the column walls. In the same type of geometry, Loutaty et al. (1969) used a velocimetry method based on the measurement of temperature profiles along the column to study water-kerosene systems. Marashino and Treybal (1971) studied a fluidized bed of different water-organic phase systems using the same measurement techniques of Weaver et al. (1959). Barnea and Mezrahi (1975) studied a butanol-brine system in a gravity settler, and measured the dispersed phase fraction by sampling the flow at different heights. Drop diameters were also measured from flow pictures analysis close to the wall and no segregation effects have been evaluated. These measurements cover a wide range of dispersed phase fraction α (0–60%), as well as particle Reynolds numbers (0.1–1,000), interfacial tension (5–48 mN/m), and viscosity ratio (0.5–5), but are all based on global velocity and phase fraction measurements. No specific measurements were attempted to characterize the homogeneity of the velocity or phase fraction fields. However, it is well known that, in a lot of industrial columns such as spray towers or fluidized beds, some large recirculations may be present that induces important local velocity and phase fraction gradients. The role of turbulence is not addressed either and the overall momentum balance accounts for these effects, which may not all be drag terms. In liquid-liquid systems at high phase fraction no local measurements for that purpose have been yet reported. In addition to accurate measurements of the local slip velocity and the phase fraction, the knowledge of the size of the inclusions is of primary importance. Compared with solid-fluid flows, the control and the measurements of the size distribution in a liquid or gas-liquid flow is more complex and the accuracy of the drop or bubble size measurements is often questionable. In the frame of a research program on dense two-phase flow modeling (Brite/Euram project No. 4322), a new measurement method has been recently developed in our laboratory to investigate dense liquid-liquid flows (Augier et al., 2000, 2001). This method allows simultaneous measurement of instantaneous velocity fields of both phases, as well as their local volume fraction and mean diameter. The principle of the measurement technique is the application of the Particle Image Velocimetry (PIV) in an optically matched liquid-liquid flow. The velocimetry is coupled with the use of a fluorescent dye to discriminate between the phases. The objective of this article is to present local measurements of the mean flow field in a homogeneous two-phase liquid cocurrent flow in order to determine the evolution of the local drag coefficient as a function of the local phase fraction. The objective is not to propose a general drag law valid in all liquid-liquid systems in any conditions, but to measure the local drag coefficient in a well defined liquid-liquid dispersion. This is made possible, because most of the terms of the momentum transport equation can be evaluated within a good accuracy. The slip velocity has been measured from dilute to concentrated dispersion up to 40% in volume. The experimental device and measuring techniques are presented, as well as the flow parameters investigated. The results are discussed and analyzed in the following section and the local drag coefficient derived from the measurements is compared with appropriate drag law correlations taken from the literature. Conclusions of that study are summarized in the last section.

Experimental Facility

Phase system

The liquid-liquid system is composed of n-heptane as the dispersed phase, and a 50% w/w water (deionized water)-glycerol mixture as the continuous phase. This system is optically homogeneous at a temperature of 29°C in order to allow the use of a noninvasive optical measuring technique such as PIV. Relevant physical properties of this phase system are reported in Table 1. No particular care has been taken to control the purity of the system and the liquid phases were

Table 1. Physical Properties of the System at 29°C.

	Density ρ (kg/m^3)	Viscosity μ (Pa·s)	Refractive Index, n_D	Interfacial Tension, σ (N/m)
n-Heptane (dispersed)	683.7	4.5×10^{-4}	1.395	31×10^{-3}
50% Glycerol-water solution	1,180	6×10^{-3}	1.395	

used as purchased. There are two main reasons for not handling this problem. First, in such a pilot, it would be a tremendous and costly effort to work in ultrapure conditions. Secondly, it is not justified in the present case because the measuring techniques developed in that study require the addition of seeding microparticles and a fluorescent dye, as explained in that section. Therefore, even in very small quantities, these products probably act as surface contaminants and tend to immobilize the interface. It is well known that even in the absence of mass transfer or surfactants, the presence of impurities at the interface may considerably affect the tangential momentum balance at the drop interface and, consequently, the resulting drag coefficient. In the case of contaminated surfaces, this drag coefficient will be larger than in the case of pure interfaces, which, in the case of a constant drag force, will lead to a decrease of the slip velocity. This point will be discussed later.

Experimental device

The experimental two-liquid phase loop is shown in Figure 1. It is a 1.4 m high vertical transparent channel with a rectangular cross-section (0.1 m $\times$ 0.2 m). The two liquid phases circulate upward cocurrently. The continuous glycerol/water phase is fed with a centrifugal pump (Lowara C0350/15) and enters the channel via a stainless steel convergent section. The dispersed phase (n-heptane) is supplied in the channel with a centrifugal pump (Someflu HMI-N) and flows through 2×400 calibrated stainless steel tubes of 1 mm in internal diameter and 42 cm length. A 2 mm-mesh grid placed in the channel section allows to maintain the capillary tubes straight aligned and ensures a good homogeneity of the continuous phase flow. At the outlet of the channel, the water/glycerol and n-heptane phases are continuously separated in a 0.3 m^3 rectangular box gravity settler before being re-introduced in the column. Flow temperature in the channel is controlled with the help of an independent water loop and an on-line heat exchanger mounted on the continuous phase circuit between the pump and the channel entrance. This heating water is also flowing inside a double jacket mounted around the gravity settler. The temperature of this water circuit is controlled with two thermal resistances and a heat exchanger supplied with an available cool glycolic solution facility (-5°C). Temperature is recorded at nine different points in the loop with the help of thermocouples and is controlled via a PID regulator acting on the thermal resistances power. With

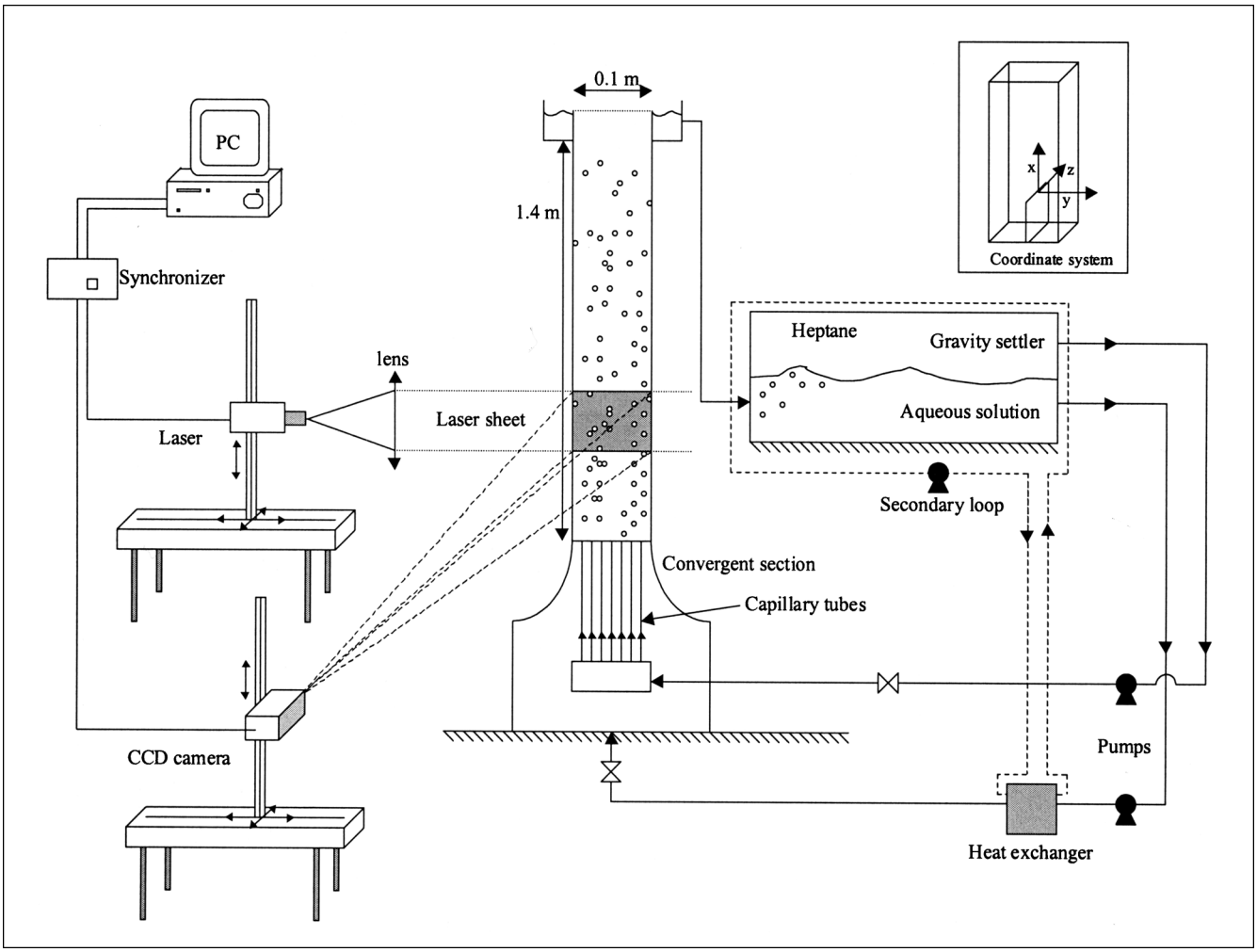

Figure 1. Experimental facility.

this system, temperature of the fluids could be maintained constant within an accuracy of 0.1°C. Flow rates of both phases are measured with the help of electromagnetic flowmeters for the continuous phase (BFP) and vortex flowmeters (Rosemount) for the heptane. Flow rates are measured within an average relative accuracy of 1% and their maximum value is 5 m^3/h for each phase. The channel walls are made of glass and poly-methylmethacrylate (pmma) allowing the crossing of the flow by a thin laser sheet and the video acquisition with a CCD camera placed perpendicularly to the sheet plane at any axial and transverse location in the column. The channel was originally designed to study mixing layer flows produced by a separation plate located at the channel bottom and dividing the inlet section in two 0.1 m $\times$ 0.1 m equal area sections. The study of homogeneous flows presented here has been achieved in a different configuration of the setup: a movable PMMA wall has been mounted in the continuation of the separation plate making a vertical channel of 0.1 m $\times$ 0.1 m square section.

Measuring Techniques

The technique developed at LGC allows simultaneous measurements of local instant two-dimensional (2-D) velocity fields of both liquid phases, as well as the phase fraction and the drop diameter in a large zone of the flow. The principle of the technique is explained in detail elsewhere (Augier et al., 2000, 2001) and has been summarized here.

Phase velocity and phase fraction measurements

The velocity measurement technique is based on a PIV method. This technique has been extensively applied to single-phase flows (Rosenfeld and Kak, 1982; Adrian, 1986, 1991), and some applications in gas-liquid and solid-liquid flows already exist (Hassan et al., 1991; Chen and Fan, 1992; Delnoij et al., 1999). The PIV technique consists in the measurement of the displacement of small seeding particles between two recorded images of the flow. In the present case, 10 μm sintered glass particles were used to seed the flow. Due to their hydrophilic properties, these particles are only present in the aqueous continuous phase and do not diffuse in the organic dispersed phase (heptane). The flow in the column is illuminated with a 0.15 m high laser sheet of approximately 0.2 10^{-3} m in thickness. The laser sheet is generated by a 20 mJ double pulsed Nd:Yag laser (Minilite from Continuum) operated at a frequency ranging between 1 and 15 Hz. The wavelength of the laser is 532 nm (green). Each pulsation is divided into two flashes separated by a delay comprised between 5 and 10^4 μs. The choice of the most suitable time interval depends upon the flow velocity. In the present case, it has been set to 4 ms. A 1,008 $\times$ 1,018 $pixel^2$ resolution black and white adapted CCD camera is used to record the flow at each flash of the laser. The CORIA Laboratory (Rouland et al., 1994) provided the PIV acquisition and processing system. The velocity of the continuous phase is measured using a cross-correlation algorithm initially developed by Willert and Gharib (1991). Recorded images are divided into square (64 $\times$ 64 px^2) interrogation windows within which the gray level cross correlation function between two consecutive images is calculated along two directions using a fast Fourier transform (FFT) algorithm. The most probable displacement of the flow in one interrogation window from one image to the next one is given by the coordinates (x,y) of the maximum peak of the cross-correlation. The accuracy of the result is increased by a Gaussian interpolation of the resulting cross-correlation peaks. Discussions about this particular point can be found in Raffel et al. (1998) and Huang et al. (1997). Although not diffusing in the dispersed phase, the glass microparticle concentration is not high enough to allow an easy discrimination between the phases. The phase discrimination is enhanced by adding to the continuous phase a very small quantity of a fluorescent dye, the Rhodamine 6G. This compound is only soluble in the aqueous water-glycerol phase, and, when excited by the laser wavelength, it emits a 560 nm wavelength orange light in the continuous phase. Therefore, in the recorded black and white images, the gray level of the continuous phase is increased by the light source, whereas the drops remain nearly black. The phase discrimination is achieved by the application of a local threshold on the gray levels. Images are divided in 100 $\times$ 100 px^2 windows inside which the gray level histograms are measured. The detection of the most frequent gray level corresponding to the Rhodamine allows to set the gray level limit under which the occurrence of the dispersed phase is detected. Using this image processing, the characteristic phase function χ_k (k is the phase index) is determined for each pixel ($\chi_k = 1$ if the phase k is present, and 0, if not). The statistical average of this function gives the phase fraction field of the dispersed phase. An illustration of this image processing algorithm is given in Figures 2a and 2b. In the raw image (Figure 2a), the gray background corresponds to the continuous phase (with the fluorescent dye) as the whiter dots represent the light reflected by the seeding particles. The dispersed phase drops appear as black dots. The gradient of illumination observed on this image justifies the use of a local threshold algorithm instead of taking a global value of the threshold. The resulting processed image is shown in Figure 2b. Apart from some limited cases, all the drops visible in Figure 2a are well reported in Figure 2b. Note that the distribution of drop projected areas in Figure 2a or 2b does not represent the actual drop size distribution, but is the result of the random crossing of the drops by the laser sheet. In addi-

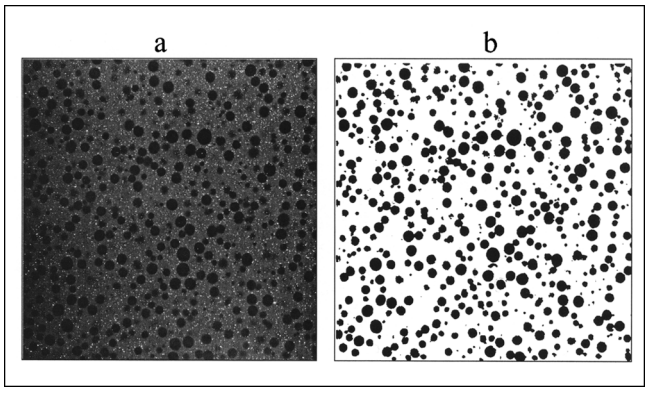

Figure 2. (a) Raw image; (b) processed image.

tion to the classical sources of errors in PIV, a fundamental question is the effect of the presence of the dispersed phase on the measurement of the continuous phase velocity. This problem has been addressed in a previous work (Augier et al., 2000) and can be briefly recalled: the first effect of the dispersed phase drop presence is to decrease the number of pixels per window occupied by the seeding microparticles. As the drops remain black, it is reasonable to think that the cross-correlation signal will have a higher noise level and the peak intensity will be altered, but not its co-ordinates. In fact, due to the displacement of the Rhodamine induced by the drop motion, the cross-correlation peak observed corresponds to the superposition of the continuous phase peak induced by the seeding particles and a wider but lower height peak corresponding to the drop velocity. The presence of this additional peak can affect the calculation of the continuous phase velocity. In order to limit this effect, the number of points taken for the sub-pixel interpolation has to be limited to three points. The dispersed phase velocity field is calculated by the same cross-correlation algorithm applied on the displacement of the inclusions in the processed images (Figure 2b). This step is similar to that presented by Hilgers et al. (1995) for gas-liquid flows. Interrogation windows have to be larger than the drops, because, in the case of a window completely occupied by the drops, the dispersed phase velocity calculation is simply not possible. When the drop phase fraction is small ($< 5\%$), it is possible to use a tracking algorithm instead of a cross-correlation function. Both techniques showed a good agreement, but the tracking (PTV) algorithm is preferable in very dilute conditions (~ 1, 2%). Figures 3a and 3b, respectively, show the continuous phase instantaneous velocity field in the middle of the column and the dispersed phase velocity field obtained at the same instant. Measurements have been performed using a 64×64 pixel^2 interrogation window with a mean dispersed phase fraction $\alpha = 27\%$. The validation of the different steps of the measurement technique has been done using both real and artificial image couples. Details can be found in Augier (2001).

Drop size measurements

Size of the drops has been measured using an image analysis of the processed images (see Figure 3b). The drop size distribution is derived from the distributions of sections between the drop and the laser sheet, following the reconstruction methods developed by Clark and Turton (1988) and by Kamp (1996). These methods have been developed in order to measure bubble diameters from chord distribution measurements in gas-liquid flows. In the present case, an image processing algorithm has been developed to discriminate and identify the different drop sections on processed images. A first result is that, in all the investigated flows, heptane drops can be considered as perfectly spherical inclusions, based on the calculation of the shape factors, which are always close to 1. Measured section distributions have been compared with section distributions generated by different types of drop diameter distributions, as monodisperse distribution, bimodal distribution, or log-normal distribution. It has then been shown that experimental drop section distributions are always very close to theoretical log-normal distributions of equation given by

$$f(d,d_{00},\sigma) = \frac{1}{\sigma d (2\pi)^{1/2}} \exp\left[- \frac{\left(\ln(d/d_{00})\right)^2}{2\sigma^2} \right] \quad (1)$$

where $f(d,d_{00},\sigma)$ is the drop size probability density function, and d_{00} and σ are the two adjustable parameters of the log-normal distribution. As an example, Figure 4a shows the probability density function (pdf) of the drop section distribution obtained with case a-4 (with an average dispersed phase fraction of 10%, see Table 2). The principle of the identification of the parameters is the following: the experimental section distribution measured in one image is divided into N classes of equivalent width. The surface fraction in each class is calculated and compared to the theoretical surface fraction resulting from the random intersection of a plane laser sheet with a spatially homogeneous drop size distribution having a

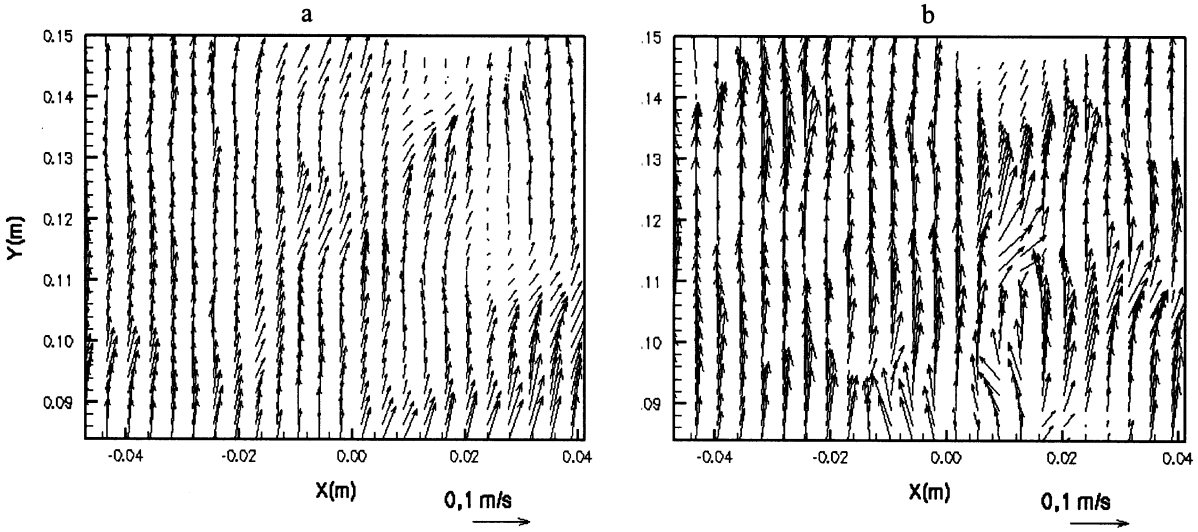

Figure 3. (a) Continuous phase instantaneous velocity field; (b) dispersed phase instantaneous velocity field.

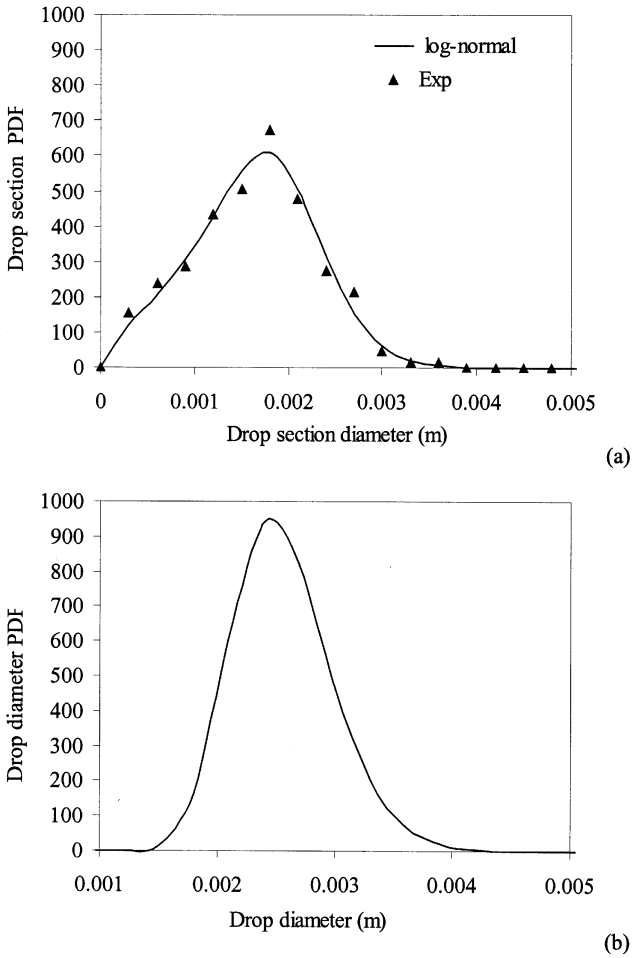

Figure 4. Probability density function of drop sections (a) and drop diameters (b); $\alpha = 22\%$.

given probability density function. Results are well fitted by a log-normal distribution with $d_{00} = 2.55$ mm and $\sigma = 0.13$. Figure 4b shows the corresponding pdf of the drop diameter distribution. This curve has been obtained from the individual labeling of 623 drop sections. The current video processing algorithm cannot discriminate between two "touching" drop sections. Such a situation occurs at high phase fraction and may induce measurement errors on the mean diameter. This error is avoided by applying a selection criterion based on the aspect ratio (aspect ratios larger than 1.1 are rejected). Due to the small value of σ, the distribution is narrow and centered around its mean value d_{00}. Calculations of surface and volume diameters d_{20} and d_{30} gives $d_{20} = 2.60$ mm and $d_{30} = 2.62$ mm. The small differences between number, surface, and volume averaged diameters suggest that the drop distribution is close to a monodisperse distribution. With a monodisperse distribution of spherical drops of diameter d, the average section diameter randomly intersecting the laser sheet is given by $\pi d/4$ if the sheet thickness is infinitely thin, and no appreciable effect results from the finite thickness (0.2 mm) of the laser sheet in the range of diameters investigated (2.5–4 mm).

Acquisition parameters

The magnification factor is 111 pixel/cm. The full image corresponds to 10 cm $\times$ 10 cm flow section area. The time step between two successive images is 4 ms. With the velocity of the continuous phase varying between 10 and 20 cm/s, this time step corresponds to a variation of the average displacement between two consecutive frames comprised between 4.5 and 9 px. Such a value may be found rather small regarding the calculation of the cross-correlation function. With the size of the window being 64×64 pixel^2, the expected value of the mean displacement is around 16 px (a quarter of the window size). Therefore, a time interval of 16 ms would seem to be more appropriate for the flow regime investigated. However, the accurate measurement of the phase fraction and the distribution of drop sections requires a low value of the thickness of the laser sheet (0.2 mm) compared to the drop diameter (2–24 mm). A larger time step involves a larger probability for the seeding particles to leave the light sheet from one image to the next. With a 4 ms time step, the error made on the displacement of the particles has been estimated around 0.1 pixel (Augier, 2001), which is quite acceptable. The pulsation of the laser source has been set to 5 Hz allowing the acquisition of five pairs of images per second.

All experiments were performed at 29 ± 0.1°C.

Flow Parameters

The values of the flow rates investigated are bounded by different constraints. The first constraint is fixed by the gravity settler ability to separate the phases at the column outlet (see Figure 1). If the total flow rate (sum of continuous and dispersed phase flow rate) is too high, the phase separation efficiency decreases and drops of organic phases are entrained into the continuous phase circuit. If it occurs, the entrained drops produce an emulsion when passing through the continuous phase pump, putting an unconditional end to the experiment. A second constraint is directly related to the achievement of a homogeneous flow, which involves a minimum continuous phase velocity in the channel section. A similar, but less severe, condition is required for the dispersed phase flow rate in order to produce a homogeneous injection of drops through the capillary network. Finally, dispersions above 40% in volume fraction do not allow a correct measurement of the continuous phase velocity (due to an impor-

Table 2. Experimental Test Cases

Test Case	a-1	a-2	a-3	a-4	a-5	a-6	a-7	b-1	b-2	b-3	b-4	b-5
Q_c (L/s)	1.056	1.056	1.056	1.056	1.056	1.056	1.056	0.913	0.913	0.913	0.913	0.913
Q_d (L/s)	0.05	0.1	0.15	0.217	0.3	0.42	0.528	0.09	0.147	0.25	0.426	—
$\bar{\alpha}$	0.021	0.051	0.082	0.10	0.172	0.225	0.278	0.05	0.15	0.22	0.38	0.001
$\bar{d}_{20}$ (m)	0.0040	0.0030	0.0026	0.0026	0.0031	0.0033	0.0040	0.0026	0.0026	0.0026	0.0026	0.0026

tant overlapping of the drop and continuous phase cross-correlation peaks). Flow parameters of experimental test cases are reported in Table 2. Homogeneous flow investigations have been carried out in a range of phase fraction varying between 0 and 40% and in a range of mean drop diameter comprised between 2.6 and 4 mm (particle Reynolds number based on terminal velocity varies between 50 and 115). Test case b-5 corresponds to the case of isolated drops at a very low concentration. The measurements were done after stopping the dispersed phase flow rate. Only a few drops were escaping from the capillary tubes for a limited period of time (a few minutes), explaining why the dispersed phase flow rate is not mentioned (close to zero); the mean phase fraction measured in this case is only an estimation. Case b-5 must be considered as a single drop experiment.

It can be observed in Table 2 that the mean diameter is not a monotonic function of the dispersed phase flow rate and also depends upon the continuous phase flow rate. The formation of drops corresponds to the breakup of a jet formed at the capillary outlet. The most frequent diameter measured was 2.6 mm, however, in cases a-1 and a-7, the mean diameter was found to be 4 mm. For the 2.6 mm diameter, the terminal velocity is 0.098 m/s and the particle Reynolds number defined as $Re_t = \rho_c d U_t/\mu_c$ is equal to 50. The Morton number of the studied liquid-liquid system defined as $M = \Delta\rho g \mu_c^4/\rho_c^2\sigma^3$ is equal to 1.5 10^{-7}. Referring to the shape regime diagram taken from the book of Clift et al. (1978), these values correspond to the limit between the spherical regime and the ellipsoidal regime with an Eötvös number equal to 1 ($E\ddot{o} = \Delta\rho g d^2/\sigma$). In fact, in the experimental range of measured diameters, the shape of the drop was always nearly spherical. Coalescence may occur in the column, but the nearly monodisperse size distribution observed suggest that this phenomenon is negligible in the range of flow parameters investigated. Apart from the jet zone at the capillary outlet, no breakup has been observed in the column.

Results and Discussion

Statistical averaging

In each interrogation window of each image (nearly 240 square cells of 64×64 pixel^2), the instantaneous volume fraction of the phase k, noted, β_k, is defined as the fraction of the window surface occupied by the phase k. Continuous and dispersed phase instantaneous velocities are computed simultaneously with β_k inside each window. This calculation is possible since the size of the windows is chosen to be larger than the average drop size (between 2 and 3 drop diameter in average). The mean phase velocity of phase k, $\vec{V}_k$, is defined as

$$V_k = \frac{\langle \beta_k \boldsymbol{v}_k \rangle}{\langle \beta_k \rangle} = \frac{\langle \beta_k \boldsymbol{v}_k \rangle}{\alpha_k} = \langle \boldsymbol{v}_k \rangle_k \quad \text{with} \quad \alpha_k = \langle \beta_k \rangle \qquad (2)$$

where the bracket symbols represent the average over the number of couple of images recorded. In the present experiments, local mean phase fraction and phase velocities have been computed over four batches of 233 couples of images, which correspond to an integration time of 47 s per batch and a total acquisition time of more than 3 min (932 couples of images). Acquisitions were collected between 15 cm and 35 cm from the bottom of the column in order to reduce the effect of the inlet conditions. Measurements were performed in the middle plan of the column in the core region of the flow (around 1 cm from the walls) in order to ensure the homogeneity of the measured profiles. Preliminary measurements showed the independence of the measurements to the transverse location of the laser sheet. The evolution of the cumulative average of the phase fraction and the phase velocities as a function of the number of acquisitions is reported in Figure 5 for the test case a-7. The average begins to stabilize after 50 pairs of images for the phase velocities whereas it takes 100 images to stabilize the mean value of the phase fraction.

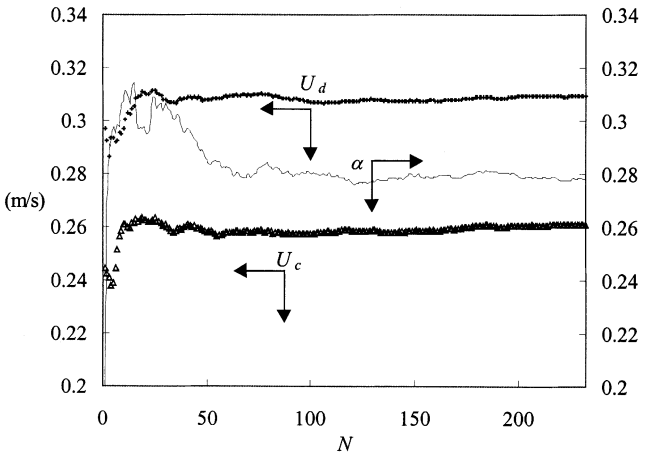

Figure 5. Cumulative average U_c, U_d, and α vs. the number of couple of images.

Mean axial velocity and phase fraction profiles

The mean axial components of the continuous and the dispersed phase velocities and the local phase fraction have been plotted in Figures 6a–6f for test cases a-1, a-2, a-5, a-6, a-7 and b-4 as a function of the transverse location, from low to high phase fraction. The profiles shown in these figures have been obtained at an axial position of 20 cm from the inlet. This distance from the dispersed phase injectors is large enough to ensure an established flow. At higher locations in the column and at a large phase fraction, large-scale recirculation patterns tend to develop and the homogeneous feature of the flow is no longer valid. In all cases, the profiles exhibit rather flat and smooth shapes with small gradients, and the velocity profiles of both phases are nearly parallel. As expected, the dispersed phase velocity is always larger than the continuous phase velocity, but the difference is decreasing with the phase fraction. However, although homogeneous, there exists a spatial distribution of averaged velocities and phase fraction for each test case studied, and consequently, a distribution of the relative velocity.

Relative velocity

The local (statistically averaged) relative velocity has been plotted in Figure 7 as a function of the local phase fraction of

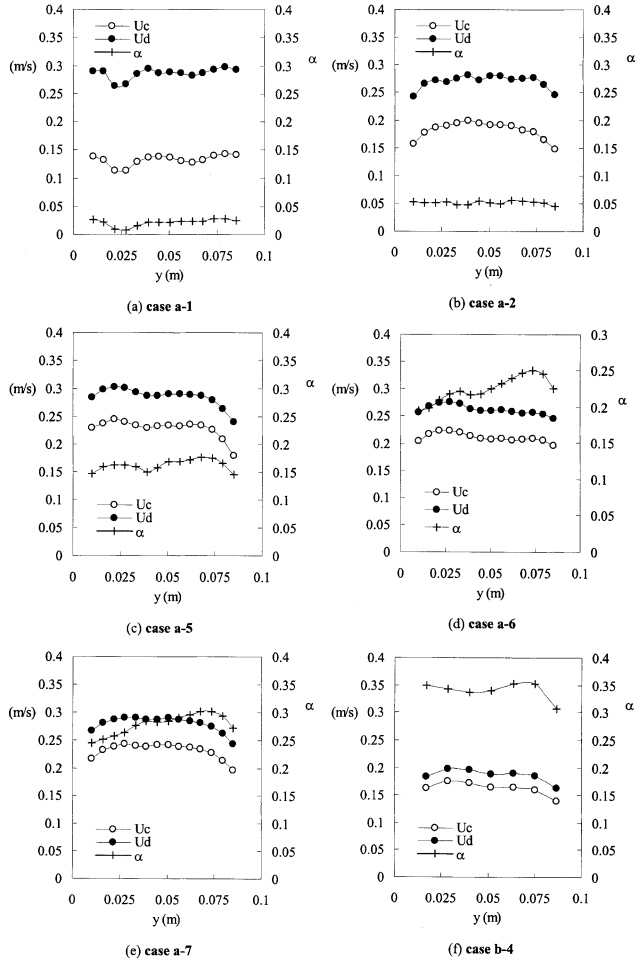

Figure 6. Phase mean axial velocity and phase fraction profiles for different test cases.

the dispersed phase. In each test case, this plot corresponds to 145 local values of α and U_r, making a total of 1,745 points for the 12 test cases investigated (measurement points close to the wall have been disregarded). The relative velocity reported in this graph is defined as the difference between the phase averaged velocity of both phases

$$U_r = U_d - U_c = \langle u_d \rangle_d - \langle u_c \rangle_c \tag{3}$$

Combined to the predominant influence of α still remains on this curve the effect of the drop diameters. In order to focus on the effect of the phase fraction, it seems relevant to normalize these values with the terminal velocity of a single drop. The first point in this graph corresponds to a value of α close to zero and a relative velocity of 0.098 cm/s (case b-5). This value is well predicted by the correlation of Schiller and Nauman (Clift et al., 1978) giving the drag coefficient of a single sphere for a Reynolds number smaller than 800

$$C_{Dt} = \frac{24}{Re_t}\left(1 + 0.15 Re_t^{0.687}\right) \quad \text{with} \quad Re_t = \frac{\rho_c U_t d}{\mu_c} \tag{4}$$

This result suggests that the drop interfaces behave as immobile interfaces, which is hardly surprising due to the presence of seeding particles and of the Rhodamine. The validity of the Schiller and Nauman correlation for single drops rising in an unbounded medium has been already observed for a broader variety of liquid-liquid systems in a previous work (Klaseboer et al., 2001). This correlation is therefore supposed to be accurately predicting the terminal velocity of drops in the range of measured diameters. Relative velocities have been normalized by the terminal velocity obtained with correlation 4 for each measured mean diameter and plotted in Figure 8 as a function of α (first value is 1 for $\alpha = 0$). The white symbols represent the averaged values of the normalized slip velocity spatially integrated over the measuring section $\overline{U}_r$. Compared with the curve of Figure 7, the dispersion of the results has been reduced, showing the importance of the diameter distribution. It must be pointed out, however, that the mean drop diameter measured in each test case is averaged over the entire measuring sections, whereas phase velocities and phase fraction are locally measured. A more accurate scaling would have been obtained with a local mea-

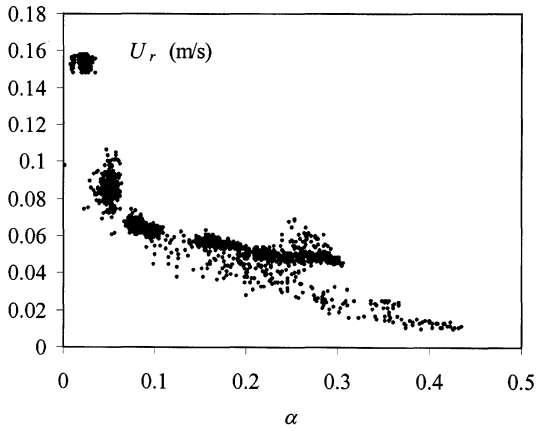

Figure 7. Absolute local mean relative velocity as a function of local phase fraction for all test cases.

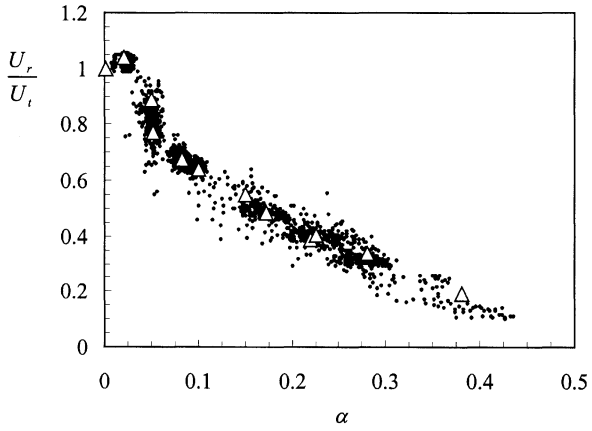

Figure 8. Normalized relative velocity as a function of the local phase fraction.

White symbols represent the relative velocity averaged over the window section.

surement of the diameter as well. However, the fact that the drop size distribution was always narrow suggests that the difference between the local mean diameter and the space-averaged diameter is probably small. Of particular interest is the left part of this curve that shows local relative velocities which are slightly larger than the terminal velocity (ratio equal to 1.04) at low α, and a rather important scattering of the normalized velocity can be observed around 5% of phase fraction. This scattering is illustrated by the amplitude of the difference (0.118) between the two averaged values obtained at 5% (case a-2 and b-1). These particular features of the relative velocity curve need to be discussed. The first explanation is the experimental uncertainty that results from the contribution of many factors as explained earlier in Klaseboer et al. (2001) (velocity, phase fraction, and diameter measurements uncertainties), which is amplified at low values of α due to the highest sensitivity of the slip velocity in that range of phase fraction. Another source of data scattering may be due to the local gradients of the mean velocity and phase fraction that needs to be evaluated. Another explanation can be found in the local structure of the instantaneous flow. The continuous phase velocity experienced by the drops is not the same everywhere in the flow at any time, due to the turbulence (mainly induced by the drops in the present case) and to the random distribution of the drops in the flow. Even if they are homogeneously distributed in average, the local formation of clusters with a finite lifetime will induce a larger fluctuation of the continuous phase velocity leading to a larger local slip velocity. If such a clustering effect occurs, the resulting slip velocity will be affected due to the fact that the phase average operator is nonlinear. The difference between the continuous phase mean velocity seen by the drops and the mean continuous phase is the "so-called" drift velocity introduced by Simonin (1991) and is given by

$$u_{dr} = \frac{\langle \beta_d u_c \rangle}{\langle \beta_d \rangle} - \frac{\langle (1-\beta_d) u_c \rangle}{1-\langle \beta_d \rangle} = \langle u_c \rangle_d - \langle u_c \rangle_c \qquad (5)$$

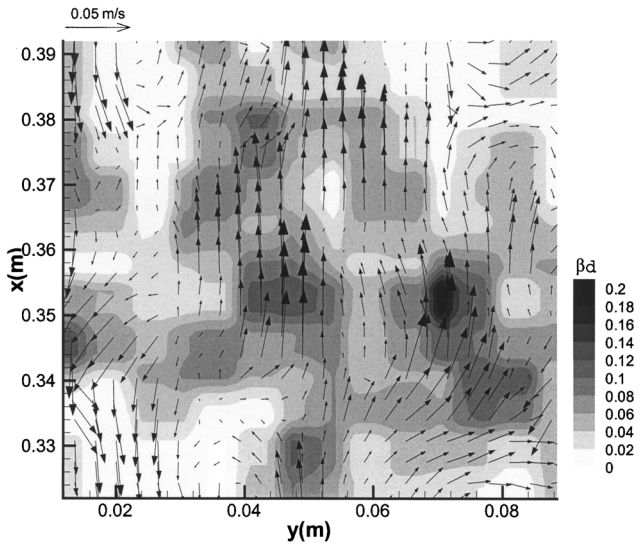

Figure 9. Instant contour plot of phase fraction density β_d and continuous phase velocity fluctuation field.

It is straightforward to show that u_{dr} is also the average of the continuous phase velocity fluctuations seen by the drops (that is, weighted by the dispersed phase density function). For an instantaneous locally homogeneous flow, the drift velocity is equal to 0. From its definition, such a quantity is difficult to evaluate and, in most of the cases, the drift velocity is either disregarded or modeled as a function of the local phase fraction gradient, as in Simonin (1991). With the current measuring technique, the drift velocity can be measured. In order to illustrate the physical meaning of the drift velocity, an instant field of the phase fraction density β_d is shown in Figure 9, corresponding to the case a-2. It can be seen in this figure that the distribution of β_d is not homogeneous, suggesting the formation of cluster or aggregate-like structures. The velocity vectors superimposed on this field represent the fluctuation of the continuous phase velocity. The correlation between the direction and amplitude of these vectors, and the excess or default of phase fraction compared to the mean value (0.051), seems obvious. Large upward vectors correspond to an aggregate-like structure, while large negative vectors correspond to a lack of drops. The mean drift velocity has been plotted as a function of α in Figure 10 for five test cases. Its value is small compared to the absolute value of the relative velocity, but significant enough to be taken into consideration, particularly at low phase fraction where it represents around 10% of the slip velocity. The drift velocity is always positive, illustrating the correlation between the continuous phase velocity fluctuations and the phase fraction density distribution observed in Figure 9. The drift velocity is rapidly decreasing as the phase fraction increases and stabilizes around 0.003 m/s for $\alpha > 0.1$. This trend seems to indicate that the existence of instantaneous phase fraction inhomogeneities has a stronger influence upon the continuous phase velocity fluctuations at the low phase fraction than at the high phase fraction. This result has some physical consistence in the sense that aggregate-like structures are expected to monitor the velocity fluctuations of the continuous phase at the low phase fraction, because they are isolated. At the higher phase fraction, even if clustering effects do exist (not shown in this article), their interactions will tend to dampen their intercorrelation with the continuous phase velocity. However, the apparent existence of a plateau in Figure 10 is not yet fully understood. Using these data, the "true" relative velocity "seen" by the drops is therefore

$$U_{r,d} = \langle u_d \rangle_d - \langle u_c \rangle_d = U_d - U_c - u_{dr} \qquad (6)$$

This relative velocity normalized by the terminal velocity has been plotted vs. α in Figure 11 in the same way as in Figure 8. The local values (black dots) have been recalculated by subtracting the drift velocity averaged in the section (it has not been calculated in all points), so the effect on the dispersion of the local values is not spectacular. In return, the effect on the space-averaged value of the relative velocity is quite significant. There is no mean relative velocity larger than 1 and the difference observed between case a-2 and b-1 in Figure 8 has been reduced by a factor 2 (0.066). The mean values of the space-averaged mean relative velocity issued from relations 3 and 6 have been summed up in Table 3 for all investigated test cases.

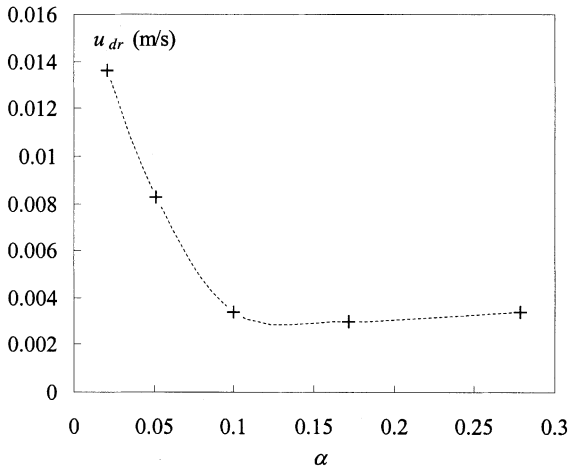

Figure 10. Drift velocity as a function of the dispersed phase fraction.

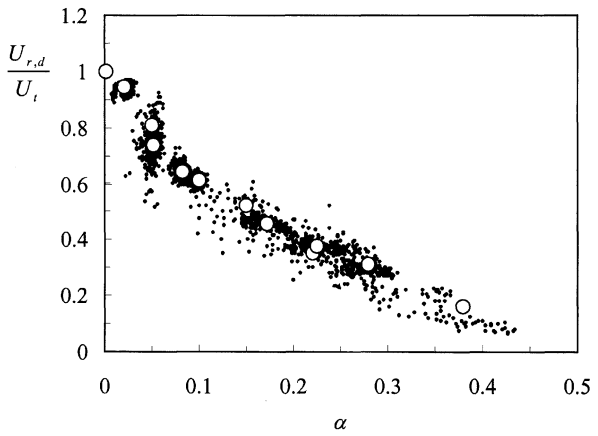

Figure 11. Normalized relative velocity seen by the drops as a function of the local phase fraction.

White symbols represent the relative velocity averaged over the window section.

The normalized space-averaged mean relative velocity has been plotted as a function of α in Figure 12a and compared with a power law of $(1-\alpha)$ (continuous line). The value of the exponent best fitting the results at low phase fraction is 4.3, leading to

$$\frac{\overline{U_{r,d}}}{U_t} = (1-\alpha)^{4.3} \tag{7}$$

However, for a phase fraction greater than 0.2, this correlation underestimates the relative velocity and an exponential function of α better fits the results in the whole range of α investigated

$$\frac{\overline{U_{r,d}}}{U_t} = \exp(-4.6\alpha) \tag{8}$$

which is represented by the dashed line in Figure 12a. This correlation is valid for the range of α studied and the question of the curve behavior at higher phase fraction is still open. However, if the values of α are reported on a semi-log scale, one can see that the normalized relative velocity is quite linear at high phase fraction and cuts the α axis at $\alpha = 0.605$, a value close to the classical maximum packing phase fraction for hard spheres (0.62). This result underlines the physical significance of this maximum packing value. The extension of the linear behavior of the experimental curve to high phase fraction of α supposes that the liquid phase still behaves like a population of nearly spherical drops. With the studied system such a condition cannot be achieved because of the increase of the coalescence rate at a high phase fraction (with the possible occurrence of phase inversion). However, for noncoalescing spherical drops, it seems reasonable to expect the extension of the linear behavior for values of α greater than 0.4. This linear behavior as a function of α log is not well reproduced by the exponential law for values of $\alpha > 0.4$. Therefore, in that range, the following law is proposed

$$\frac{\overline{U_{r,d}}}{U_t} = 0.834\log\left(\frac{\alpha_m}{\alpha}\right) \quad \text{with} \quad \alpha_m = 0.605 \tag{9}$$

Equation 9 has been drawn in Figure 12b (cross symbols) in the range $0.025 < \alpha < 0.6$. It is interesting to notice that the evolution of the normalized slip velocity is well represented by this law for values of α as low as 0.1. This value roughly corresponds to the theoretical value of α at which the mean distance between particles (in tetrahedral packing) is equal to the particle diameter. This result supports the idea that, in dispersed flows, 10% is the transition value of the phase fraction between a dilute and a concentrated behavior.

Drag coefficient

The derivation of a local drag coefficient law as a function of α and particle Reynolds number from the above results requires the existence of a local equilibrium between the

Table 3. Space-Averaged Mean Relative Velocity with Drift Effect ($\overline{U_{r,d}}$) and without ($\overline{U_r}$)

Test Case	a-1	a-2	a-3	a-4	a-5	a-6	a-7	b-1	b-2	b-3	b-4	b-5
$\overline{\alpha}$	0.021	0.051	0.082	0.10	0.172	0.225	0.278	0.05	0.15	0.22	0.38	0.001
$\overline{d}_{20}$ (m)	0.004	0.0030	0.0026	0.0026	0.0031	0.0033	0.0040	0.0026	0.0026	0.0026	0.0026	0.0026
$\overline{U_r}$ (m/s)	0.155	0.087	0.066	0.063	0.056	0.05	0.05	0.087	0.054	0.038	0.021	0.098
$\overline{U_{r,d}}$ (m/s)	0.141	0.079	0.063	0.06	0.053	0.047	0.0836	0.051	0.0510	0.0346	0.016	0.098
$\overline{U_r}/U_t$	1.040	0.770	0.673	0.643	0.483	0.403	0.336	0.888	0.551	0.388	0.194	1
$\overline{U_{r,d}}/U_t$	0.946	0.740	0.643	0.612	0.457	0.376	0.313	0.806	0.520	0.363	0.159	1
Re_p	110.9	49.3	32.3	30.7	32.3	30.2	36.7	40.4	26.1	17.7	8	50.1

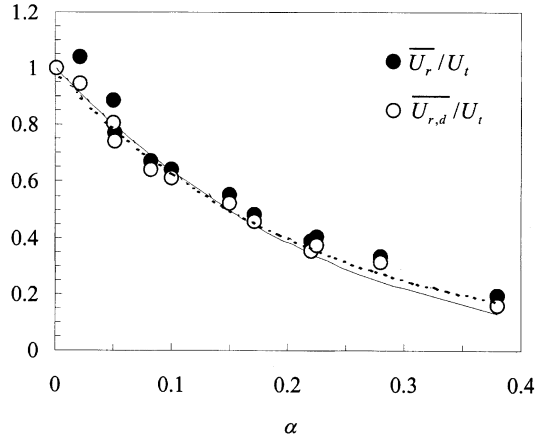

(a)

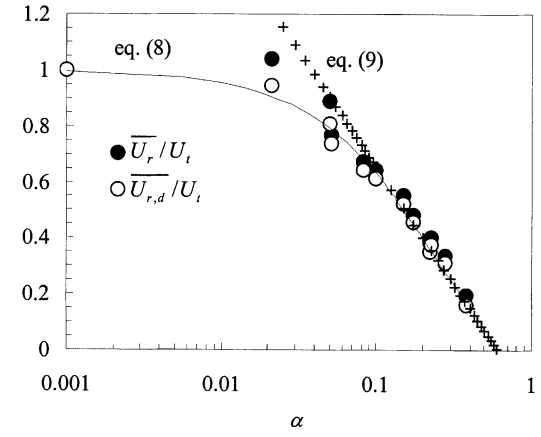

(b)

Figure 12. Evolution of normalized values of $\overline{U_r}$ and $\overline{U_{r,d}}$ as a function of α.

(a) Continuous line is obtained from Eq. 7 and dotted line is obtained from Eq. 8. (b) Continuous line is obtained from Eq. 8 plotted between $\alpha = 0$ and $\alpha = 0.4$. Cross symbols are obtained from Eq. 9 plotted between $\alpha = 0.02$ and $\alpha = 0.605$.

buoyancy and the interfacial drag force, that is, that other forces play a negligible role. To identify the drag independently from other forces, the condition of local homogeneity has to be fulfilled. In order to evaluate such a force balance, the different terms in the momentum equation of conservation of both phases need to be evaluated. This equation reads in each phase

$$\alpha_k \rho_k \frac{\partial}{\partial t}\mathbf{V}_k + \alpha_k \rho_k \mathbf{V}_k \cdot \nabla \mathbf{V}_k = -\alpha_k \nabla \mathbf{P} + \alpha_k \rho_k \mathbf{g} - \nabla \cdot (\alpha_k \rho_k \langle \mathbf{v}_k'' \mathbf{v}_k'' \rangle_k) + \mathbf{I}_k \quad (10)$$

where $\mathbf{V}_k$ and $\mathbf{v}_k''$ are the phase-averaged mean and fluctuating velocities of phase k, P is the pressure supposed to be the same in each phase. Note that, as a first approximation, the granular pressure term in the dispersed phase equation has been neglected, as well as the laminar and collisional tensors, so that momentum diffusion is supposed to be driven only by the Reynolds stress contribution. $\mathbf{I}_k$ is the interfacial momentum transfer between the phases ($\mathbf{I}_c + \mathbf{I}_d = 0$). The pressure gradient term of Eq. 10 can be eliminated by multiplying Eq. 10 by $(1-\alpha_k)$ and subtracting the dispersed phase momentum equation for $k = d$ to that of the continuous phase ($k = c$) leading to the resulting equation

$$\begin{aligned}(1-\alpha)\alpha\left(\rho_c \frac{\partial}{\partial t}\mathbf{V}_c - \rho_d \frac{\partial}{\partial t}\mathbf{V}_d\right) &+ (1-\alpha)\alpha(\rho_c \mathbf{V}_c \cdot \nabla \mathbf{V}_c - \rho_d \mathbf{V}_d \cdot \nabla \mathbf{V}_d) \\ &= (1-\alpha)\alpha \mathbf{g}(\rho_c - \rho_d) - \alpha \nabla \cdot ((1-\alpha)\rho_c \langle \mathbf{v}_c'' \mathbf{v}_c'' \rangle_c) \\ &+ (1-\alpha)\nabla \cdot (\alpha \rho_d \langle \mathbf{v}_d'' \mathbf{v}_d'' \rangle_d) + \mathbf{I}_c \quad (11)\end{aligned}$$

The time-dependent term appearing in Eq. 11 accounts for the large-scale fluctuations of the mean velocity. The evaluation of this term strongly depends on the size of the low-pass time scale filter applied on the velocity signal. This term could be evaluated by applying a sliding average of a given length (20, 30 couples of images) on an acquisition batch, provided that the phase average of both phase velocity fluctuations is equal to zero. As we deal with stationary variables in this variable, this term simply cancels. Equation 11 can be further simplified by taking into consideration only the axial component of this equation. This is justified by the fact that the flow has been checked to be essentially unidirectional. The local mean transverse velocity component does not exceed 5% of the axial component in all test cases and the advective contribution of this term in Eq. 11 can be disregarded (see Figure 13a). Measurements of fluctuating components of the Reynolds stress tensor showed that the diagonal terms are at least an order of magnitude larger than the tangential part; this result is illustrated in Figure 13b. Therefore, the axial component of Eq. 11 reduces to

$$\begin{aligned}I_{cx} &= (1-\alpha)\alpha g(\rho_c - \rho_d) \\ &\quad \text{(I)} \\ &+ (1-\alpha)\alpha\left(\rho_c U_c \frac{\partial U_c}{\partial x} - \rho_d U_d \frac{\partial U_d}{\partial x}\right) \\ &\quad \text{(II)} \\ &+ \rho_c \alpha \frac{\partial((1-\alpha)\langle u_c'' u_c'' \rangle_c)}{\partial x} - \rho_d (1-\alpha)\frac{\partial(\alpha \langle u_d'' u_d'' \rangle_d)}{\partial x} \quad (12) \\ &\quad \text{(III)}\end{aligned}$$

The first term of the righthand side of Eq. 12 is the buoyancy term (I), the second is the advective term (II), and the last term (III) is the turbulence induced diffusivity term (IV). The lefthand side term represents the axial component of the interfacial momentum transfer between the phases and is the summation of a stationary drag term and an added mass term

$$I_{cx} = \alpha \rho_c \frac{3C_D}{4d} u_{r,d} |V_{r,d}| + \alpha \rho_c C_{AM}\left(U_d \frac{\partial U_d}{\partial x} - U_c \frac{\partial U_c}{\partial x}\right) \quad (13)$$
$$AM$$

where d is the local mean diameter of the drops, C_D is the drag coefficient, and C_{AM} is the added mass coefficient. A

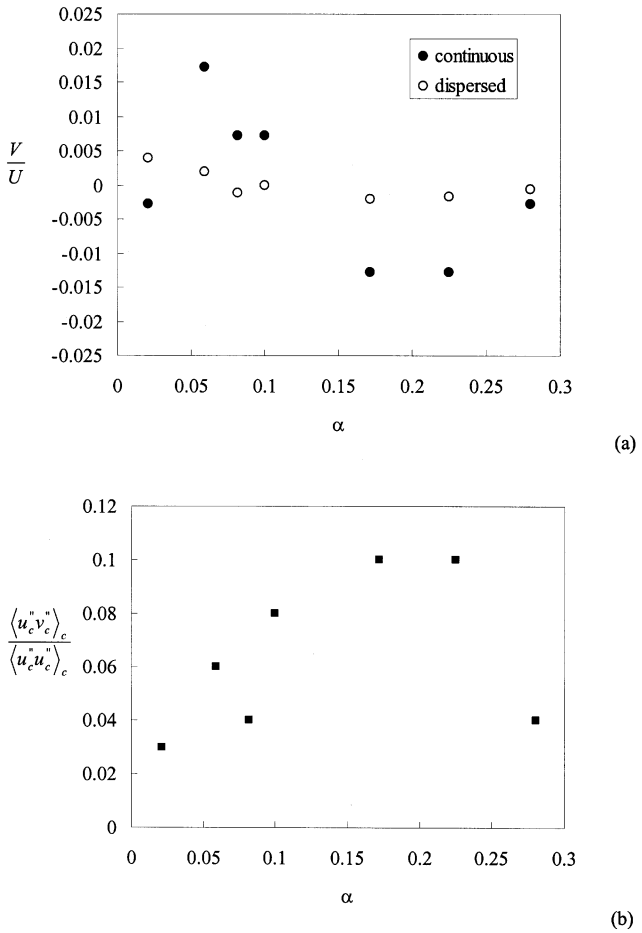

Figure 13. (a) Transverse-to-axial velocity ratio for both phases at different α; (b) continuous phase Reynolds stress tensor tangential to normal component ratio as a function of α.

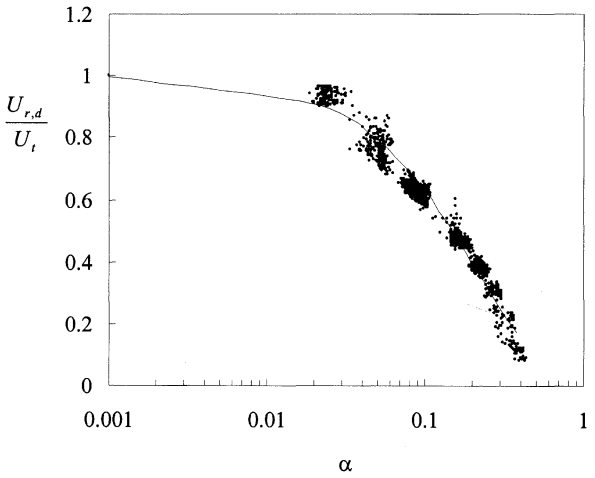

Figure 14. Filtered local relative normalized velocity as a function of α.

Black line curve is Eq. 8 ($e^{-4.6\alpha}$).

true estimate of the added mass force requires the knowledge of the added mass coefficient as a function of the phase fraction. It is equal to 0.5 for a single spherical drop and it has been shown to increase with increasing phase fraction in suspensions of solid spheres, as shown by Felderhof (1991). According to the law proposed by this author, in the range of phase fraction investigated (0–0.4), C_{AM} varies between 0.5 and 2 (for $\alpha = 0.4$). As the drops are spherical with quasi-immobile interfaces, we will consider in the first approximation that the amplitude of variation of the added mass coefficient has the same order of magnitude in our experimental test cases. From all the local measurements, it is thus possible to calculate all the terms of Eqs. 12 and 13 in order to check the condition of equilibrium between the interfacial drag term and the buoyancy term. This local calculation of the different terms allows to consider only the local slip velocity data, which correspond to this equilibrium within an accuracy of 10%. The drag and the added mass term are expressed as a function of the mean velocity of both phases. As both of these terms are nonlinear, turbulent contributions may be accounted for in both of these forces and would be included into the drag or added mass coefficient if they are not accounted for explicitly. Therefore, in order to limit the fluctuations the interfacial terms due to the existence of a local gradient of the velocity fluctuations, for a given test case, data corresponding to the same level of fluctuations have been conserved. The resulting plot of $U_{r,d}/U_t$ corresponding to these filtering operations is shown in Figure 14. Note that this filtering effect has eliminated some of the most distant points from the space-averaged values in Figure 11, which is a result that gives support to the validation of the measuring technique. This filtering operation has not significantly modified the space-averaged values of the slip velocity and the exponential law of Eq. 8 is unchanged. The remaining dispersion band can be probably due to the uncertainty on the phase fraction measurement and to the approximation of the local diameter by a space-averaged diameter over the full image section. The contribution of the different terms of Eqs. 12 and 13 (I, II, III, AM and the buoyancy term) is estimated by evaluating the sum of their maximum absolute values. The ratio between the drag term and the buoyancy term resulting from this evaluation is reported in Figure 15. Its maximum value is 1.12 at low concentration of the dispersed phase and tends towards 1 as α is increasing. The local drag coefficient can therefore be correctly estimated by the following relation

$$C_D = (1-\alpha)\frac{4d\Delta\rho g}{3\rho_c \overline{U_{r,d}}^2} \tag{14}$$

Note that this equation supposes that the absolute value of the relative velocity can be assimilated to that of the axial component, a simplification that has been already verified (see Figure 13a). The local relative velocity has been also identified to its space-averaged value, provided that the local dispersion is not caused by the turbulence gradients or by inertia effects. Substituting in relation 14 the value of the mean diameter and of the relative velocity gives a relationship between the drag coefficient and the local phase fraction α and the terminal velocity. Introducing the drag coefficient

of a single drop (at $\alpha = 0$),

$$C_{Dt} = \frac{4d\Delta\rho g}{3\rho_c U_t^2} \tag{15}$$

leads to

$$\frac{C_D}{C_{Dt}} = (1-\alpha)\left(\frac{U_t}{U_{r,d}}\right)^2 \tag{16}$$

Using correlation 8 and 9, the final expression for the drag coefficient ratio reads

$$C_D = C_{Dt}(1-\alpha)\exp(9.2\alpha) \text{ in the range } 0 < \alpha < 0.4 \tag{17}$$

or

$$C_D = 1.438 C_{Dt}(1-\alpha)\left[\log\left(\frac{\alpha_m}{\alpha}\right)\right]^{-2} \quad \text{for } 0.1 < \alpha < \alpha_m = 0.605 \tag{18}$$

Correlation 17 has been tested against five drag coefficient models or correlations proposed in the literature which have been selected regarding the validity of their application to the present system. These models have been reported in Table 4.

Some of these correlations are more specific to solid-fluid-systems, such as the correlations of Wallis (1974) and Wen and Yu (1966). The choice of these models is driven by the probable condition of immobile interface in the present experiments. The correlation proposed by Ishii and Zuber (1979) corresponds to the viscous undistorted regime. The transition to the distorted regime is given by an upper limit of the Morton number as a function of the Eötvös number. According to this criterion, this limit is reached in our system with a drop diameter larger than 3.5 mm. Therefore, the undistorted viscous regime applies for all the investigated test cases, except for cases a-1 and a-7 where the drop mean diameter is 4 mm. However, experimental observations suggested that even in those cases, the drop shape is spherical and undistorted, so the same correlation has been evaluated for these cases. For the same explanation of interfacial immobility, in both the correlations of Ishii and Zuber (1979) and of Barnea and Mezrahi (1975), the dispersed phase viscosity should be taken large before the continuous phase viscosity, although it is obviously not the case ($\mu_d/\mu_c = 0.075$). The mixture viscosity used for these correlations is therefore simplified into the following relations

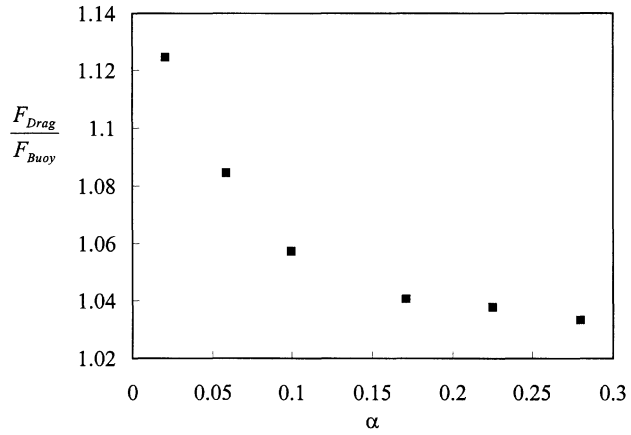

Figure 15. Maximum absolute discrepancy between the drag force and the buoyancy force as a function of α.

$$\mu_m = \mu_c \exp\left(\frac{5\alpha}{3(1-\alpha)}\right) \tag{19}$$

for the Barnea and Mezrahi's correlation and

$$\mu_m = \mu_c\left(1-\frac{\alpha}{\alpha_m}\right)^{-2.5\alpha_m} \quad \text{with} \quad \alpha_m = 0.62 \tag{20}$$

for the Ishii and Zuber's correlation.

Table 4. Drag Coefficient Models

Ref.	Drag Law
Kumar and Hartland (1985)	$C_d = \left(K_1 + \frac{24}{Re}\right)(1 + k\alpha^n)$ with $K_1 = 0.53$; $k = 4.56$; $n = 0.73$
Ishii and Zuber (1979)	$C_d = \frac{24}{Re_m}(1 + 0.1 Re_m^{0.75})$; $Re_m = \frac{\rho_c d U_r}{\mu_m}$; $\mu_m = \mu_c\left(1-\frac{\alpha}{\alpha_m}\right)^{-2.5\alpha_m\frac{\mu_d+0.4\mu_c}{\mu_d+\mu_c}}$
Barnea and Mezrahi (1975)	$Cd = (1+\alpha^{1/3})\left(0.63 + \frac{4.8}{\sqrt{Re_m}}\right)^2$ with $Re_m = \frac{\rho_c d U_r}{\mu_m}$, $\mu_m = \mu_c K_b \frac{\frac{2}{3}K_b + \frac{\mu_d}{\mu_c}}{K_b + \frac{\mu_d}{\mu_c}}$
	$K_a = \frac{\mu_c + 2.5\mu_d}{2.5\mu_c + 2.5\mu_d}$, $K_b = \exp\left(\frac{5\alpha K_a}{3(1-\alpha)}\right)$
Wallis (1974)	$C_d = C_{d0}(1-\alpha)^{3-2n}$; $n = 4.7\frac{1+0.15Re^{0.687}}{1+0.253Re^{0.687}}$; $Re = \frac{\rho_c D U_r}{\mu_c}$
Wen and Yu (1966)	$C_d = \frac{24}{Re}(1+0.15\mathrm{Re}^{0.687})(1-\alpha)^{-1.7}$; $Re = \frac{(1-\alpha)\rho_c d U_r}{\mu_c}$

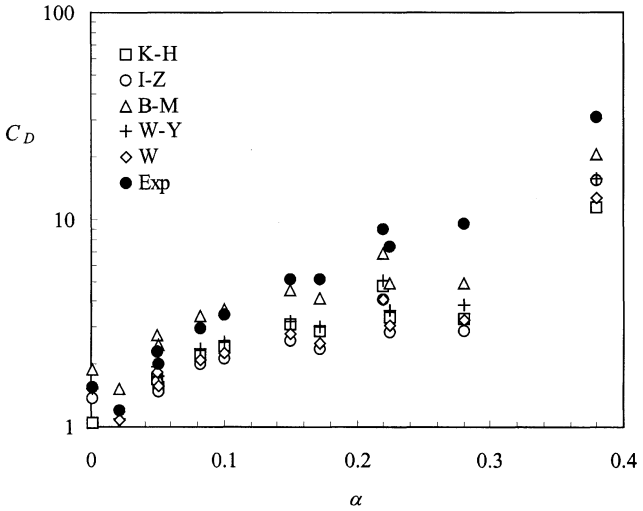

Figure 16. Drag coefficient based on local measurements of $\overline{U_{r,d}}$, d_{20}, and α (K–H) Kumar and Hartland (1985); (I–Z) Ishii and Zuber (1979); (B–M) Barnea and Mizrahi (1975); (W) Wallis (1974); (W–Y) Wen and Yu (1966).

Black circles are our experimental data.

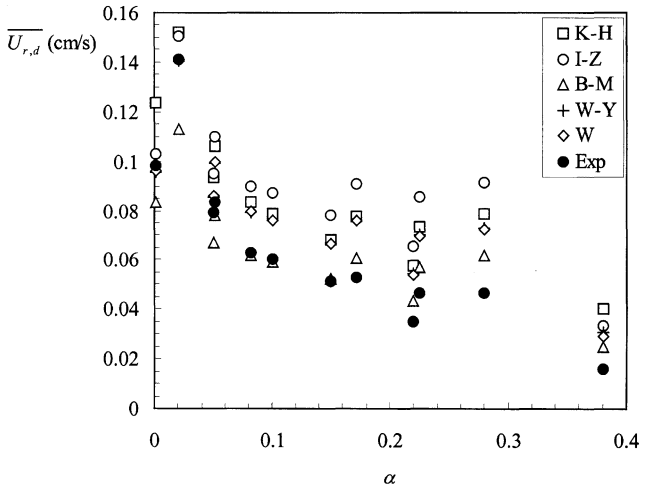

Figure 17. Relative velocity as a function of α derived from local equilibrium assumption.

Same legend as in Figure 16.

Note that the value of the maximum packing fraction proposed by the authors has been conserved, although they recommend taking $\alpha_m = 1$ in the case of droplet flows. This choice of $\alpha_m = 0.62$ is consistent with the "hard sphere" behavior of our system in the range of the phase fraction investigated and corresponds to the theoretical numerical value of α_m (0.605) that cancels the slip velocity, obtained by simple extrapolation of the normalized slip velocity curve (Figure 12b). The correction term $(1+\alpha^{1/3})$ that accounts for wall effects in the Barnea and Mezrahi's correlation should be disregarded in our case, but their mixture viscosity model has been fitted from experimental data accounting for this correction term. Therefore, in order to keep the consistency between the drag coefficient and the mixture viscosity models of Barnea and Mezrahi, the wall effect correcting factor has to be included in the calculation of the drag coefficient. The laws reported in Table 4 apply for a large range of particle Reynolds number and phase fraction that include the range of flow parameters of the present investigation. The first evaluation consists in computing the drag coefficient obtained with these laws using the local measurements of the slip velocity $\overline{U_{r,d}}$, α and the mean diameter d_{20}. The resulting plot is reported in Figure 16 and compared to the experimental correlation (Eq. 17). This figure shows that the present data are underestimated by all the models for $\alpha > 0.1$, with the best agreement being observed with the correlation of Barnea and Mezrahi. In Figure 17, the relative velocity obtained with these models assuming local equilibrium between the drag and the buoyancy forces has been plotted as a function of α with the present liquid-liquid system. Again here the best prediction is observed with the correlation of Barnea and Mezrahi, except in the case of dilute dispersion. Other laws significantly overpredict the measured relative velocity. Since the values at the origin are not the same for all correlations, a normalized representation of C_D by the drag coefficient of a single sphere C_{Dt} (obtained by taking $\alpha = 0$ in the different models) gives a better evaluation of the different models on our data, in particular the important underestimation of this ratio at the high phase fraction shown in Figure 18. Even if correlations never provide an exact value of every experimental set of data, it can be said that the trend of all these drag coefficient models does not represent well the evolution of the experimental drag coefficient as a function of α. Moreover, the best agreement is found with the correlation of Barnea and Mezrahi that accounts for a wall effect that shouldn't be considered with the studied system. These correlations include the combined effect of the phase fraction and of the particle Reynolds number, as well as the experimental correlation Eq. 17. Also, the discrimination between the effect of phase fraction and the particle Reynolds number is not an easy task. In the limit of low Reynolds number (creeping flow), it has been shown (Ishii and Zuber, 1979) that the general form of the mixture viscosity for rigid particles could be written as Eq. 20. Other theoretical relations have been derived by Hawksley and Vand (Barnea and Mezrahi, 1975)

$$\mu_m = \mu_c \exp\left(\frac{-2.5\alpha}{(1-0.609\alpha)}\right) \tag{21}$$

and by Happel, whose numerical calculation can be approximated by the following equation (Barnea and Mezrahi, 1975)

$$\mu_m = \mu_c \exp(-4.58\alpha) \tag{22}$$

In the creeping flow regime, the relative velocity is well predicted using Eq. 16

$$\frac{\overline{U_{r,d}}}{U_t} = (1-\alpha)\left(\frac{\mu_c}{\mu_m}\right) \quad \text{with} \quad Re \ll 1 \tag{23}$$

Experimental data obtained in that regime are well predicted by Eqs. 20 or 21 (Hanratty and Bandukwala, 1957).

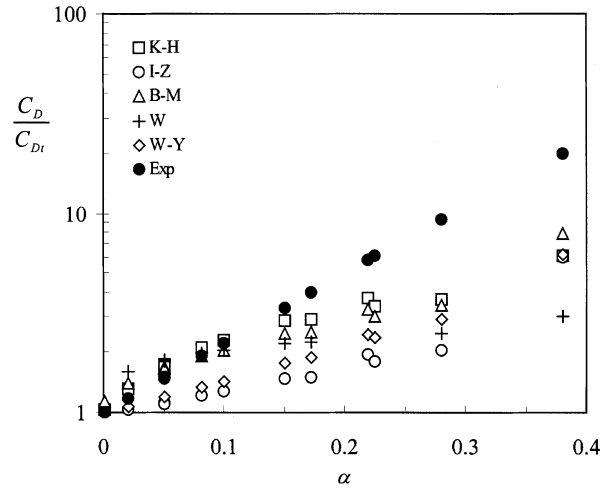

Figure 18. C_D/C_{Dt} as a function of α.

Same legend as in Figure 16.

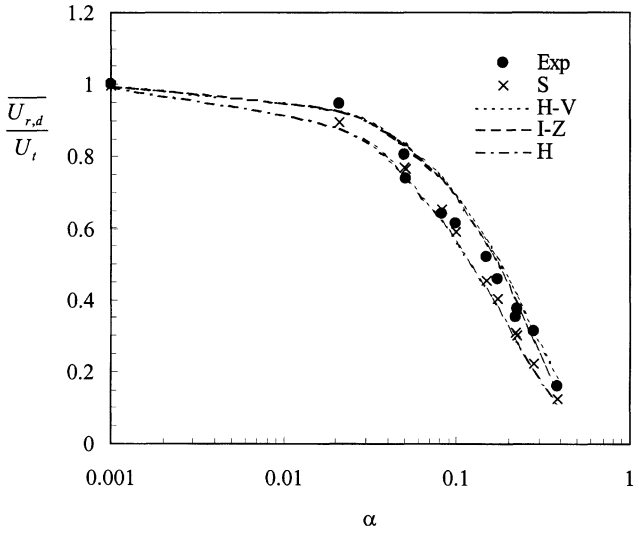

Figure 19. Comparison of measured normalized slip velocity (black circles) as a function of α with creeping flow mixture viscosity models.

Hawkskley and Vand (H–V); Steinour (S); Ishii and Zuber (I–Z); Happel (H).

The evolution of the normalized relative velocity measured with the present system has been compared to that given by relation 23, using Eqs. 20 and 21 for the mixture viscosity equation. The results are plotted in Figure 19 and show a much better agreement than those obtained with the two-phase drag coefficient laws available at higher Reynolds number. In particular at high phase fraction, the coincidence between the theoretical laws and present data is quite good. Overall, the Hawskley and Vand's law and Ishii's law slightly overestimate the experimental points as the Happel's model tends to underestimate them. The experimental correlation obtained by Steinour (Barnea and Mezrahi, 1975) for settling spheres in the creeping flow range has also been reported in this graph. It is probably the best fit of the present data. Such

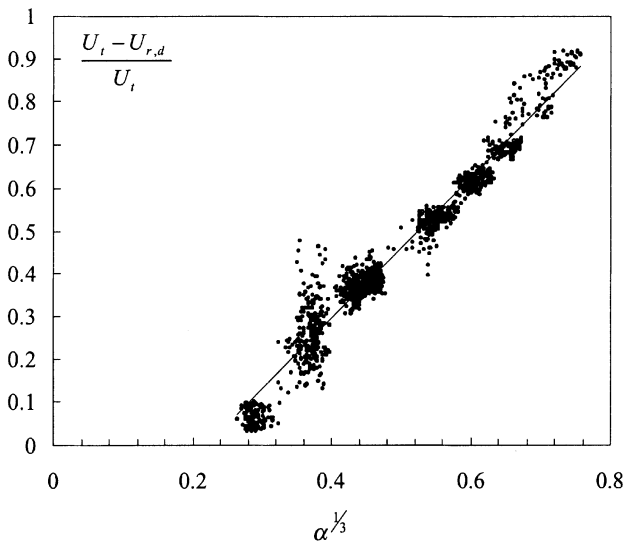

Figure 20. Evolution of the hindrance factor as a function of α.

a result suggests that the effect of the phase fraction in the creeping flow regime is very similar to that observed in the viscous regime in a range of larger particle Reynolds number (10–100) and brings a theoretical background of correlations 17 and 18. According to our results, these laws are valid for particle Reynolds numbers as high as 100 and offer a much better prediction than the drag coefficient laws as a function of the two-phase particle Reynolds number in the viscous regime.

Following Garnier et al. (2001), this behavior similarity observed with settling suspensions suggests that at high phase fraction in a homogeneous flow, the interparticle distance

$$E_h = \frac{U_t - U_{r,d}}{U_t} \tag{24}$$

Assuming the interparticle distance to vary like $d\alpha^{-1/3}$, Garnier et al. have found a perfect linear dependence between the above hindrance factor and $\alpha^{1/3}$ in the case of dense homogeneous bubble flows. The range of volume fraction investigated by these authors is identical to the current one (between 0.01 and 0.4), but the particle Reynolds number is much larger, ranging between 1,000 and 1,500. In the same way, we have plotted in Figure 20 the evolution of the hindrance factor vs. $\alpha^{1/3}$. The result is very close to that observed by Garnier et al., supporting the idea of similarity of buoyancy-driven dispersed flow at a high phase fraction with settling suspensions, independently of the particle Reynolds number.

However, the experimental relation found for C_D in Eq. 17 cannot be used as a local drag law that could be implemented in a calculation code. For a single drop, the stationary drag laws of the literature have been established on the base of measurements at terminal velocity. Then, it is assumed that the relation between the drag coefficient and the particle Reynolds number at terminal velocity is unchanged whatever the relative velocity is. Hence, the Shiller and Nauman's law is commonly applied even in a nonuniform flow field (where

other forces are present). Following this process, the extension of the drag law (Eq. 17) would take the following form in a nonuniform flow

$$C_D = C_{D0} F(\alpha) \quad \text{with} \quad C_{D0} = f(Re_p)$$

$$\text{and} \quad Re_p = \frac{d\overline{U_{r,d}}\rho_c}{\mu_c} \qquad (25)$$

where $F(\alpha)$ is a function of α that has to be determined. In the equation above, the coefficient C_{D0} is the coefficient of a single drop with slip velocity $U_{r,d}$. It is assumed in relation 25 that the function $f(Re_p)$ is the Shiller and Nauman law as in the case of a single drop. Doing so, relation 25 is consistent with the commonly accepted drag law of a single drop in a nonuniform flow (that is, when α tends towards zero). In the general case, there is not a *univocal* relation between $U_{r,d}$ and α as in the case of a steady homogeneous flow (present case). However, relation 25 must be consistent with this case and $F(\alpha)$ can be determined from the present experiments. The best fitting law found is

$$F(\alpha) = e^{5.2\alpha} \quad \text{in the range} \quad 0 < \alpha < 0.4 \quad \text{and with}$$

$$Re_p < 100 \qquad (26)$$

Conclusion

The accurate measurement of the local relative velocity in a homogeneous liquid-liquid flow as a function of the local phase fraction has allowed to derive a local two-phase drag coefficient verifying the equilibrium between the buoyancy and the drag force. Results showed that in the range of particle Reynolds number investigated (viscous regime), the classical drag coefficient laws underestimate the effect of the phase fraction on the drag coefficient, and, as a consequence, overestimate the measured relative velocity, particularly at a high phase fraction. In return, the measured drag coefficient can be written as the product of the single drop drag coefficient and a function of the local phase fraction which is well predicted by the theoretical mixture viscosity models in the creeping flow regime. Such a result has been obtained with nearly spherical drops behaving like rigid particles for values of the phase fraction ranging between 0 and 0.4. Further development of that work needs to focus on higher particle Reynolds number. However, the measurement technique accuracy is limited at this time to the case of weakly deformed drops.

Acknowledgments

This work was achieved in the frame of a research project Brite/Euram No. 4322 financed by the European Community and was also supported by the French National Council for Scientific Research (CNRS).

Literature Cited

Adrian, R. J., "Multi-Point Optical Measurements of Simultaneous Vectors in Unsteady Flow—a Review," *Int. J. Heat Fluid Flow*, **7**, 127 (1986).

Adrian, R. J., "Particle-Imaging Techniques for Experimental Fluid Mechanics," *Ann. Rev. Fluid Mech.*, **23**, 261 (1991).

Augier, F., O. Masbernat, and P. Guiraud, "Simultaneous Volume Fraction and Velocity Measurements in Liquid-Liquid Flows," *Proc. of FEDSM'00* (2000).

Augier, F., J. Morchain, P. Guiraud, and O. Masbernat, "Volume Fraction Gradient Induced Flow Patterns in a Two-Liquid Phase Mixing Layer," *Proc. 4th Int. Conf. on Multiphase Flow*, New Orleans (2001).

Augier, F., "Structure Locale du Champ Hydrodynamique dans les Ecoulements Dispersés Liquide-liquide Concentres," These de doctorat de l'Institut National Polytechnique de Toulouse, France (2001).

Barnea, E., and J. Mizrahi, "A Generalized Approach to the Fluid Dynamics of Particulate Systems. Part 2: Sedimentation and Fluidization of Clouds of Spherical Liquid Drops," *Can. J. Chem. Eng.*, **53**, 461 (1975).

Chen, R. C., and L. S. Fan, "Particle Image Velocimetry for Characterizing the Flow Structure in Three-Dimensional Gas-Liquid-Solid Fluidized Beds," *Chem. Eng. Sci.*, **47**, 3615 (1992).

Clark, N. N., and R. Turton, "Chord Length Distributions Related to Bubble Size Distributions in Multiphase Flows," *Int. J. Multiphase Flow*, **14**, 4, 413 (1988).

Clift, R., J. R. Grace, and M. E. Weber, *Bubbles, Drops, and Particles*, Academic Press, London (1978).

Delnoij, E., J. Westerweel, N. G. Deen, J. A. M. Kuipers and W. P. M. van Swaaij, "Ensemble Correlation PIV Applied to Bubble Plumes Rising in a Bubble Column," *Chem. Eng. Sci.*, **54**, 5169 (1999).

Felderhof, B. U., "Virtual Mass and Drag in Two-Phase Flow," *J. Fluid Mech.*, **225**, 177 (1991).

Garnier, C., M. Lance, and J. L. Marié, "Measurements of Local Flow Characteristics in Buoyancy-Driven Bubbly Flow at High Void Fraction," *Proc. of ICMF'01*, (2001).

Garwin, L., and B. D. Smith, "Liquid-Liquid Spray Tower Operation in Heat Transfer," *Chem. Eng. Process*, **49**, 11, 91 (1953).

Geankoplis, C. J., J. B. Sapp, F. C. Arnold, and G. Marroquin, "Axial Dispersion Coefficients of the Continuous Phase in Liquid-Liquid Spray Tower," *I&EC Fund*., **21**, 306 (1982).

Hanratty, T. J., and A. Bandukwala, "Fluidization and Sedimentation of Spherical Particles," *AIChE J.*, **3**, 2, 293 (1957).

Hassan, Y. A., T. K. Blanchat, C. H. Seeley, Jr., and R. E. Canaan, "Simultaneous Velocity Measurements of Both Components of a Two-Phase Flow Using Particle Image Velocimetry," *Int. J. Multiphase Flow*, **18**, 3, 371 (1991).

Hazlebeck, D. E., and C. J. Geankoplis, "Axial Dispersion in a Spray Extraction Tower," *I&EC Fund*., **2**, 4, 310 (1963).

Hilgers, S., W. Merzkirch, and T. Wagner, "PIV Measurements in Multiphase Flow Using CCD- and Photo-Camera," *Flow Visual. Image Process. of Multiphase Systems*, FED-Vol. **209**, ASME, 151 (1995).

Huang, H., D. Dabiri, and M. Gharib, "On Errors on Digital Particle Image Velocimetry," *Meas. Sci. Technol.*, **8**, 12, 1427 (1997).

Ishii, M., and N. Zuber, "Drag Coefficient and Relative Velocity in Bubbly, Droplet or Particulate Flows," *AIChE J.*, **25**, 5, 843 (1979).

Kamp, A., "Ecoulements Turbulents à Bulles dans une Conduite en Micropesanteur," Thèse de doctorat, INPT, Toulouse, France (1996).

Klaseboer, E., J. P. Chevaillier, A. Mate, O. Masbernat, and C. Gourdon, "Model and Experiments of a Drop Impinging on an Immersed Wall," *Phys. Fluids*, **13**, 1, 45 (2001).

Kumar, A., and S. Hartland, "Gravity Settling in Liquid-Liquid Dispersions," *Can. J. Chem. Eng.*, **63**, 368 (1985).

Kumar, S. B., M. P. Dudukovic, and B. A. Toseland, "Measurement Techniques for Local and Global Fluid Dynamic Quantities in Two and Three Phase Systems," *Non-Invasive Monitoring of Multiphase Flows*, Chaouki et al., eds., Elsevier Science B. V., **1**, 45 (1996).

Loutaty, R., A. Vignes, and P. Le Goff, "Transfert de Chaleur et Dispersion Axiale dans une Colonne à Pulvérisation Liquide-Liquide en Lit Lâche et en Lit Dense," *Chem. Eng. Sci.*, **24**, 1795 (1969).

Marashino, M. J., and R. E. Treybal, "The Coalescence of Drops in Liquid-Liquid Fluidized Beds," *AIChE J.*, **17**, 11, 1174 (1971).

Mudde, R. F., and O. Simonin, "Two and Three-Dimensional Simu-

lations of a Bubble Plume Using a Two-Fluid Model," *Chem. Eng. Sci.*, **54**, 5061 (1999).
Raffel, M., C. Willert, and J. Kompenhans, *Particle Image Velocimetry*, Springer (1998).
Rosenfeld, A., and A. C. Kak, *Digital Picture Processing*, 2nd ed., **1**&**2**, Academic Press, Orlando, FL (1982).
Rouland, E., S. Vottier, B. Lecordier, and M. Trinité, "Cross-Correlation PIV Development for High Speed Flows with a CCD Camera," *Proc. 2nd Int. Seminar on Opt. Methods and Data Processing in Heat and Fluid Flow*, London (1994).
Rusche, H., and R. I. Issa, "The Effect of Voidage on the Drag Force on Particles in Dispersed Two-Phase Flow," *Proc. of JETFM* (2000).
Simonin, O., "Prediction of the Dispersed Phase Turbulence in Particle-Laden Jets," *Proc. 4th Int. Symp. on Gas-Solid Flows, ASME FED*, **121**, 197 (1991).
Viollet, P., and O. Simonin, "Modeling of Turbulent Two-Phase Jets Loaded with Discrete Particles," *Phenomena in Multiphase Flow*, Hewitt et al., eds., p. 259, Hemisphere (1990).
Wallis, G. B., "The Terminal Speed of Single Drops or Bubbles in an Infinite Medium," *Int. J. Multiphase Flow*, **1**, 491 (1974).
Weaver, E. C. R., L. Lapidus, and J. C. Elgin, "The Mechanics of Vertical Moving Liquid-Liquid Fluidized Systems: I. Interphase Contacting of Droplets Passing through a Second Quiescent Fluid," *AIChE J.*, **5**, 5, 533 (1959).
Wen, C., and Y. Yu, "Mechanics of Fluidization," *Chem. Eng. Prog. Symp. Ser.*, **62**, 100 (1966).
Willert, C. E., and M. Gharib, "Digital Particle Image Velocimetry," *Exp. Fluids*, **10**, 181 (1991).

Manuscript received July 30, 2001, revision received Aug. 12, 2002, and final revision received Apr. 21, 2003.